DEVELOPMENT AND APPLICATION OF DISTRIBUTED MEMS PRESSURE SENSOR ARRAY FOR AUV OBJECT AVOIDANCE

Vicente I. Fernandez vicentef@mit.edu
Stephen M. Hou shou@mit.edu
Franz S. Hover hover@mit.edu
Jeffrey H. Lang lang@mit.edu
Michael S. Triantafyllou mistetri@mit.edu

Massachusetts Institute of Technology
77 Massachusetts Avenue
Cambridge MA, 02139

July 23, 2009

Abstract

A novel sensory system is being developed for AUVs to augment current sensory systems for navigation and operation in difficult environments. These environments are frequently cluttered and murky with substantial flow from currents or waves, frustrating sonar and vision systems while posing an increased risk to AUVs. In order to manage such situations, a better ability to locate and identify physical objects is needed. This gap could be filled by small low frequency pressure sensors distributed over the surface of the AUV in dense arrays.

The pressure sensor array presented here consists of hundreds of MEMS pressure sensors with diameters near 1 mm spaced a few millimeters apart fabricated on etched silicon and Pyrex wafers; a fabrication process for producing the array is described. A strain-gauge pressure sensor is analyzed, fabricated, and tested. It satisfies specifications as required for object detection. The sensing element is a strain gauge mounted on a flexible diaphragm, which is a thin (20 μm) layer of silicon attached at the edges to a square silicon cavity 2000 μm wide on a side. A source voltage of 10 V produces a sensor with a sensitivity on the order of 1 μV/Pa. Since the thermal noise voltage is near 0.7 μV, the pressure resolution of the sensors is on the order of 1 Pa.

In addition to a pressure sensor array capable of measuring the spatial pressure distribution, progress has also been made in estimating the shape of an arbitrary two-dimensional physical object in a flow and in tracking vortices based solely on distributed pressure measurements. The shape estimation relies on a conformal mapping which orders shape parameters by their observability with range. Utilizing this model, a sequential maximum likelihood estimation technique is able to extract the contour of an object in steady flow. This procedure requires no a priori knowledge of the type of object. The result is an estimate of a completely arbitrary shape whose level of generality depends on the distance of the object.

[1]This publication is the result of research sponsored by The MIT Sea Grant College Program, under NOAA grant number NA06OAR4170019, project number R/RT-2/RCM-17.

1 Introduction

Fish, which manage complex environments with the aid of their lateral line organs, inspired this sensor type. In particular, the blind Mexican cavefish (Astyanax fasciatus) is able to navigate its environment relying almost exclusively on this organ. The lateral line is a sensory system which measures the flow velocity and pressure distribution over the fish's surface, providing sufficient information for surprising behaviors. The most relevant of these behaviors are collision avoidance (Windsor et al. 2009) and object recognition (Campenhausen et al. 1981). These behaviors are related to a particular subset of the lateral line organ, which measures only the pressure gradient (Montgomery et al. 2001). It is still poorly understood how fish extract relevant environmental information from pressure gradients. We report progress in fabricating a sensor array capable of measuring similar quantities as the lateral line organ, and in utilizing the pressure measurements to extract detailed information about solid objects and flow structures using statistical inference techniques.

While an implementation identical to the lateral line organ is not practical, the information provided by the lateral line would greatly benefit AUVs. In particular, the ability to locate and obtain information about nearby obstructions is increasingly important as AUV's are finding applications in cluttered environments and surf zones. Also, the ability for flow mapping and identifying vortical structures allows the possibility for opti-

mizing control and navigation in unsteady environments. In addition to these capabilities, a distributed pressure sensor would be completely passive and consequently require little power. The primary disadvantage would be its limited range.

Described here is the development of a sensor inspired by the canal system of the lateral line organ. This sensor attempts to directly extract information from the spatial pressure fields using an array of pressure sensors. This bypasses the pressure gradient to flow transformation of the canal system, considerably simplifying the design while possibly losing some favorable filtering characteristics [1]. The development of a full MEMS pressure sensor array, experiments with off-the-shelf sensors, and signal processing are subsequently considered in order to create a sensor system able to identify and classify nearby objects.

2 MEMS Pressure Sensor Array Development

The pressure sensor array presented here consists of hundreds of MEMS pressure sensors with diameters near 1 mm spaced a few millimeters apart fabricated on etched silicon and Pyrex wafers; the sensors are arranged over a surface in various configurations, such as a single line, a patch consisting of several parallel lines (as shown in Figure 1), or specialized forms to fit the hull shape of a vehicle or its fins.

2.1 Membrane Design

The key feature of the sensor is a flexible diaphragm, which is a thin (20 μm) layer of silicon attached at the edges to a silicon cavity. A strain gauge consisting of four long and thin snaking resistors sits on the surface of the diaphragm. As the difference in pressure above and below the diaphragm changes, the diaphragm bends and the strain gauge resistances change. The four resistors are optimally designed and connected in a Wheatstone bridge configuration to maximize the pressure sensitivity. A schematic side view of one sensor is shown in Figure 2. These design requirements are within the scope of MEMS technology.

2.2 Stress, Strain, and Pressure

To express the strain in one of the resistors as a function of the pressure on the diaphragm, let L be the length of the side of the square diaphragm and H be its thickness. Following [2, 3], the normal displacement $\hat{w}$ of the diaphragm as a function of its horizontal x and y coordinates is approximated as a function of the form

$$\hat{w}(x,y) = \frac{c_1}{4}\left[1+\cos\left(\frac{2\pi x}{L}\right)\right]\left[1+\cos\left(\frac{2\pi y}{L}\right)\right], \tag{1}$$

where the origin is the center of the plate and c_1[1] is the deflection at the center of the diaphragm. The resulting pressure-deflection relation is

$$P = \frac{\pi^4 E H^3}{6(1-\nu^2)L^4} c_1, \tag{2}$$

where P is the pressure difference across the diaphragm, E and ν are the Young's modulus and the Poisson's ratio for the diaphragm, respectively. As calculated in [4] using finite-element methods, the stress in the x-direction is

$$\sigma_x = 0.294\left(\frac{L}{H}\right)^2 P. \tag{3}$$

Given $L = 2000\,\mu\mathrm{m}$ and $H = 20\,\mu\mathrm{m}$ as typical membrane sizes, the stress is

$$\sigma_x = 2940 \cdot P. \tag{4}$$

As shown in [5], the strain in the x direction is

$$\begin{aligned}\epsilon_x &= K\left(\frac{L}{H}\right)^2\left(\frac{P}{E}\right)\left(\frac{z}{H}\right)\left[\cos\left(\frac{2\pi x}{L}\right)\right] \\ &\quad\cdot\left[1+\cos\left(\frac{2\pi y}{L}\right)\right],\end{aligned} \tag{5}$$

where z is the vertical position within the membrane relative to the center plane, and it can be shown that the relative change in resistance for a resistor segment deformed by being bonded to the top of such a plate is

$$\frac{\Delta R}{R} \approx \frac{1}{1-\nu}\epsilon_l + \frac{2\nu-1}{1-\nu}\epsilon_w, \tag{6}$$

where ϵ_l and ϵ_w are the strains along the resistor length and width, respectively.

2.3 Deflection and Sensitivity

The maximum deflection c_1 of the diaphragm, which occurs at the center, is

$$c_1 = \frac{K}{\pi^2}\left(\frac{P}{E}\right)\left(\frac{L^4}{H^3}\right). \tag{7}$$

[1] The subscript in c_1 refers to the fact that it is the amplitude of the first mode of vibration for the diaphragm. This paper does not discuss other modes, but the notation is used for consistency with other works.

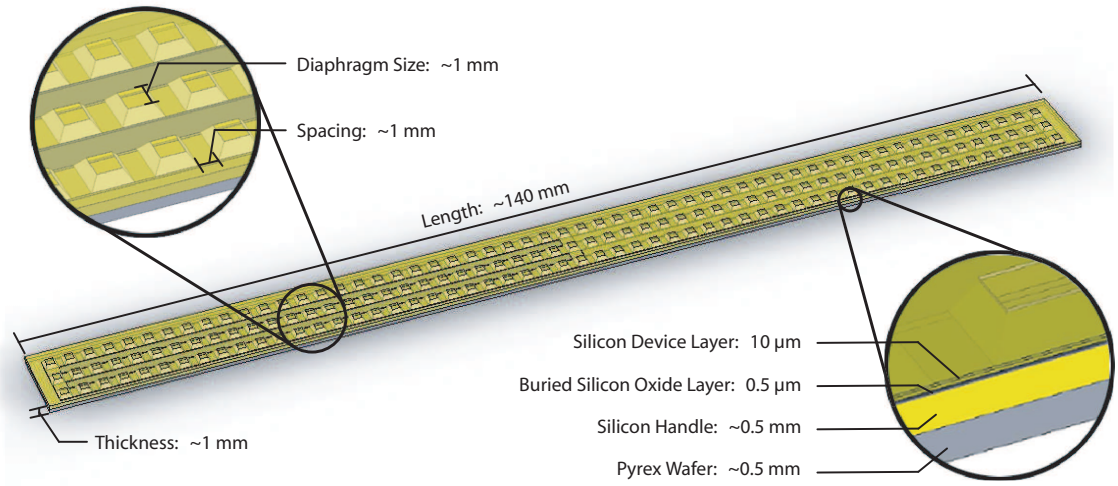

Figure 1: Diagram of pressure-sensor array with basic structure depicted.

The maximum strain in the x direction, which also occurs at the center, is

$$\epsilon_x = 2K\left(\frac{L}{H}\right)^2\left(\frac{P}{E}\right)\left(\frac{z}{H}\right). \tag{8}$$

By symmetry, the strain the y direction is the same. For $K = 0.294$, $E = 47\,\mathrm{GPa}$ (silicon), $L = 2000\,\mu\mathrm{m}$, and $H = 20\mu\mathrm{m}$, these quantities become

$$\frac{\epsilon_i}{P} = 1.25 \times 10^{-7}\,\mathrm{Pa}^{-1} \tag{9}$$

$$\frac{c_1}{P} = 1.3\,\mathrm{nm/Pa}. \tag{10}$$

Substituting the value given in Equation 9 into Equation 6 produces the relative change in resistance:

$$\frac{\Delta R}{R} \approx \left(1.07 \times 10^{-7}\,\mathrm{Pa}^{-1}\right) \cdot P. \tag{11}$$

Thus, for a typical source voltage of $V_s = 10\,\mathrm{V}$ for the Wheatstone bridge, the sensitivity of a strain-gauge resistor sensor located at the center of the diaphragm is on the order of $1\,\mu\mathrm{V/Pa}$.

2.4 Noise

Thermal noise voltage is on the order of

$$V_N = \sqrt{4kTRf}, \tag{12}$$

where k is Boltzmann's constant, T is temperature, R is resistance, and f is the filtered bandwidth of the electrical signal [2]. Thus, for $T = 300\,\mathrm{K}$, $R = 10\,\mathrm{k\Omega}$, and $f = 3\,\mathrm{kHz}$, the thermal noise voltage is $0.7\ \mu\mathrm{V}$.

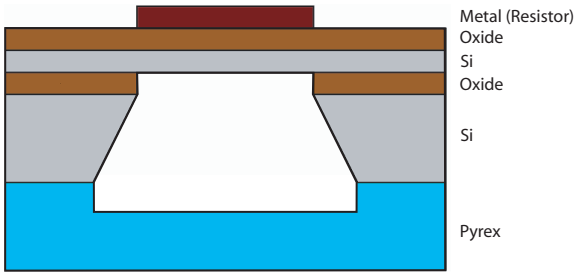

Figure 2: Sideview of the fabrication layers of a single sensor (not to scale). The portion of the silicon and oxide layers above the etched hole is the diaphragm.

Therefore, the pressure sensitivity of the sensors is on the order of 1 Pa for a 10 V source, which is the level needed for the aforementioned applications.

2.5 Fabrication

The fabrication of a basic pressure sensor array is described here. The steps were performed in the MIT Microsystems Technology Laboratories and can be done with standard CMOS/MEMS processes.

A double-side polished silicon-on-insulator (SOI) wafer, which contains a 20 μm thick Si layer to be used as the diaphragm, is first masked with a silicon-nitride (Si_3N_4) layer. The nitride is removed from the device/diaphragm side, oxide is grown on the bare silicon to act as an insulating layer, and the metal resis-

tors are deposited on the oxide. The diaphragms are patterned on the backside nitride. The backside of the SOI wafer is then etched using potassium-hydroxide (KOH) with the nitride as a mask and the original SOI oxide as an etch stop to form an air cavity. During KOH etching, the metal resistors and oxide on the front side are protected by a double O-ring seal and teflon wafer holder. The remaining Si_3N_4 mask is then dry etched away to expose silicon. In the meantime, a Pyrex glass wafer is laser etched to create shallow valleys that allow air to pass. The Pyrex and SOI wafers are then anodically bonded to form arrays of the devices shows in Figure 2.

2.6 Results

A wafer set consisting of nine nearly identical columns of sensors was fabricated. The two columns at either side of the wafer are different from the others in that they have two fewer sensors. Each column consists of ten sensors; two each of diaphragm size 1 mm, 1.41 mm, 2 mm, 2.42 mm and 4 mm. The ten sensors in each column share a single air cavity, and the ten air cavities are isolated from one another. One diaphragm from each column is broken and glued to a copper tube. A manometer is attached to the copper tubes, which enable us to control the back pressure on a column of sensors. Since the manometer is water-based, the range and resolution of differential pressure between atmospheric pressure on the top of the diaphragms and the back pressure on the bottom is determined by the size of the manometer. We can produce pressure differences between -1500 Pa and 1500 Pa with a precision of 10 Pa.

2.6.1 Diaphragm thickness measurement

A scanning electron microscope (SEM) photograph of the diaphragm cross-section was taken (Figure 3) and the thickness of the diaphragm was measured to be 18.2 μm, about 10% thinner than the nominal 20 μm.

2.6.2 Deflection measurements

The deflection of the center of the membrane away from equilibrium was also measured as a function of pressure. These measurements were obtained from a Zygo profilometer. Figure 4 shows the profile of a 2.8 mm diaphragm at a pressure of -2900 Pa. The green line in the lower-left graph is the profile of a cross-section of the diaphragm, the location of which is indicated by the white line in the upper-left color plot. Figure 5 shows the results from two diaphragms of sizes 2 mm and 2.828 mm. The experimental deflections are 0.51 nm/Pa and 2.54 nm/Pa, respectively. The theoretical values are 1.26 nm/Pa and 5.07 nm/Pa, respectively, for a diaphragm of 20 μmand are 1.67 nm/Pa and 6.73 nm/Pa, respectively, for a diaphragm of 18.2 μm. The factor of 3 difference between theory and experiment could be the result from several possible sources. For example, the oxide grown and metal deposited on the diaphragm occurred under high temperature and low pressure, respectively. These processes pre-stressed the diaphragm layers to alter the deflection-pressure characteristics.

2.6.3 Voltage measurements

The strain-gauge resistors on the diaphragms are individually tested. To test a resistor, it was used as one of the resistors in an external Wheatstone bridge system. A voltage source powers the configuration, and the output of the bridge is fed into an AD620 low-power instrumentation amplifier from Analog Devices, Inc. with a gain of 960. The output of the amplifier is read on a voltmeter and oscilloscope. First, we tune the Wheatstone bridge by adjusting a potentiometer in the bridge until the output is zero voltage under zero pressure difference. Next, the output of the amplifier is measured as the back pressure produced by the manometer is varied.

From the amplified voltage, we can calculate the relative change in resistance $\Delta R/R$ for the strain-gauge resistors as functions of pressure. Figure 6 shows a such a plot for each of the four strain-guage resistors on a particular diaphragm with a width of 2.82 mm. As expected, two of them vary positively with pressure and the other two vary negatively. The experimental values of $(\Delta R/R)/P$ are $-2.94 \times 10^{-7}\,\mathrm{Pa}$, $-2.78 \times 10^{-7}\,\mathrm{Pa}$, $2.52 \times 10^{-7}\,\mathrm{Pa}$ and $2.65 \times 10^{-7}\,\mathrm{Pa}$. However, the theoretical value is $\pm 1.07 \times 10^{-7}\,\mathrm{Pa}$. There are several possible explanations for the discrepancy between theory and experiment.

One contributor to the discrepancy is that the diaphragm, which is nominally $20\,\mu\mathrm{m}$ thick, is in fact 18.2 μm thick. This difference could be due to manufacturing variations from the vendor (the specifications state that the thickness is precise to within $1\,\mu\mathrm{m}$) or to slight overetching from the KOH. Since sensitivity is inversely related to the square of the diaphragm thickness, small changes in the thickness can have a significant effect on the sensitivity. In this case, the recalculated sensitivity is $\pm 1.29 \times 10^{-7}\,\mathrm{Pa}$. This is closer to the experimental values than is the nominal calculation.

Another is that the diaphragms had been stretched and deformed somewhat during the fabrication process,

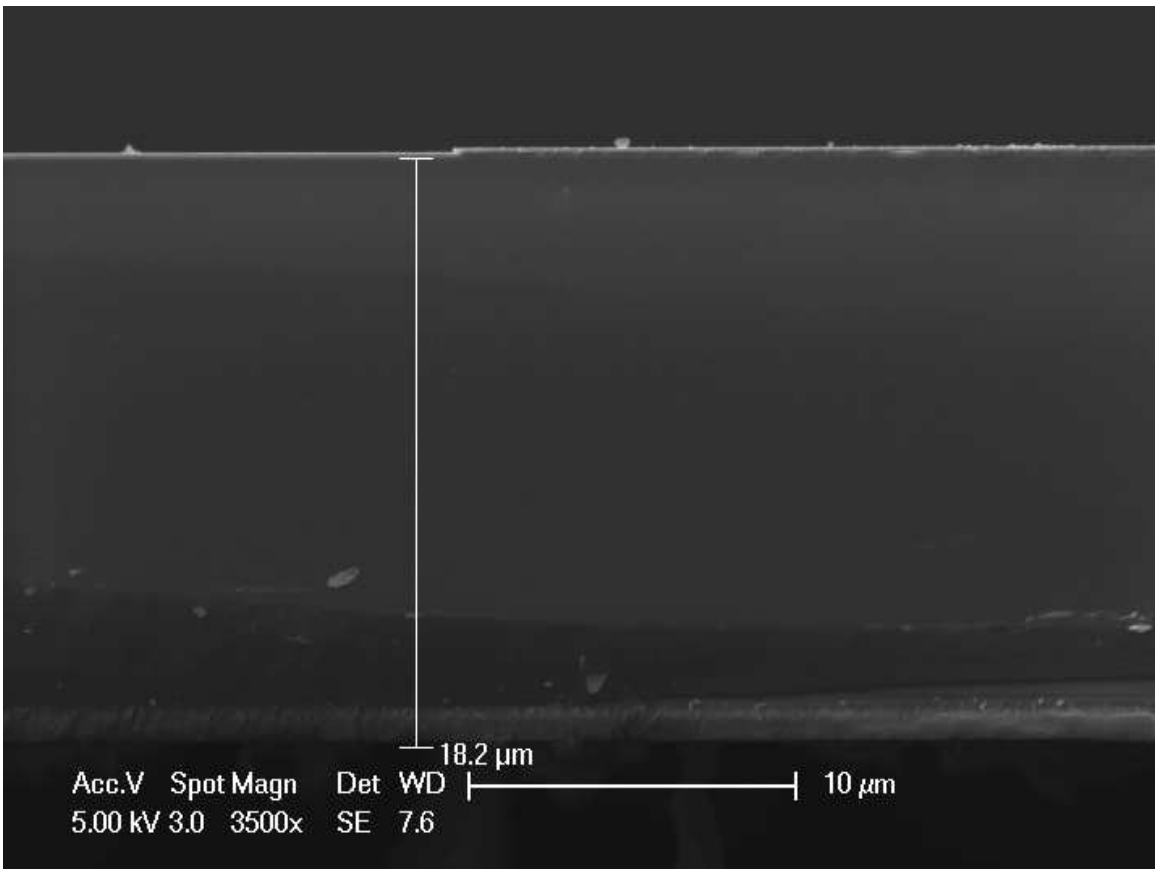

Figure 3: SEM photograph of the cross-section of a diaphragm.

which has several steps in which the wafer is placed under varying pressures from a vacuum to atmospheric pressure. As stated earlier, the larger membranes were permanently plastically deformed. Perhaps the smaller ones were affected as well, though not to the same degree as the larger ones. In any case, the sensitivity of the sensor is better than we had designed them to be.

2.7 Underwater sensors

The results presented above demonstrate that a silicon-based strain-gauge sensor is a viable technology for an AUV pressure sensor. Thus, the next generation of sensors was fabricated as well. In this set, the sensors are no longer isolated and are instead wired up on-chip in a Wheatstone bridge configuration. The sensors are powered up and accessed via a custom-made cable system that makes contact with the silicon wafer at one end. In this set, 23 sensors sit at the top of a 150-mm wafer. All consist of 2 mm square diaphragms and are 2 mm apart. Parylene is added to the top layer of the wafer as a waterproofing material. The wafer is mounted onto a plastic holder for support and control of flow. The entire system can then be placed underwater to detect local changes in pressure. Figure7 shows a photograph of the mounted system.

The system is currently being tested underwater.

3 Conclusion

We have demonstrated a silicon-based strain-gauge pressure sensor fabricated with standard MEMS techniques that can be suitably used for underwater object detection and estimation. The noise floor after amplification was measured to be a few millivolts. Thus, both the mechanical deflection and electrical tests indicate that a sensitivity on the order of Pascals can be achieved. The experiments show that 2 mm wide diaphragms are both sensitive and robust enough for our purposes and thus would be the standard size for future testing and the development of a larger-scale system.

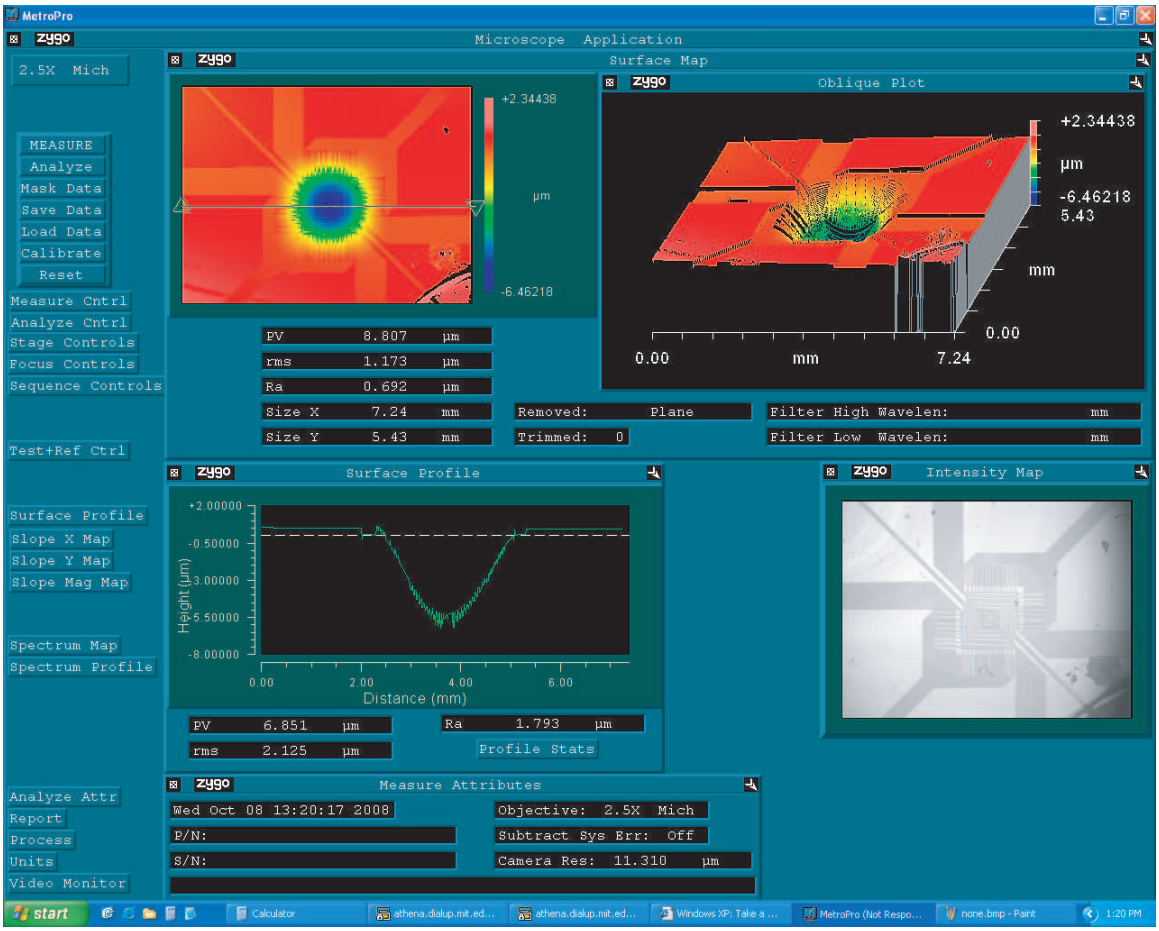

Figure 4: Profiles of a 2.8 mm diaphragm at a pressure of -2900 Pa as measured by a Zygo profilometer

.

References

[1] S. M. van Netten. Hydrodynamic detection by cupulae in a lateral line canal: Functional relations between physics and physiology. *Biological Cybernetics*, 94:67–85, 2006.

[2] S. D. Senturia. *Microsystem Design*. Kluwer Academic Publishers, Boston, Massachusetts, 2001.

[3] V.I. Fernandez, S.M. Hou, F.S. Hover, J.H. Lang, and M.S. Triantafyllou. Lateral line inspired MEMS-array pressure sensing for passive underwater navigation parts I & II. In *Proc. of the 2007 International Symposium on Unmanned Untethered Submersible Technology*. Autonomous Undersea Systems Institute, August 2007.

[4] S. K. Clark and K. D. Wise. Pressure sensitivity in anisotropically etched thin-diaphragm pressure sensors. *IEEE Transactions on Electronic Devices*, 26(12):1887–1896, December 1979.

[5] S. Timoshenko. *Theory of Plates and Shells*. McGraw-Hill Book Company, Inc., New York, New York, second edition, 1959.

[6] C. B. Braun and S. Coombs. The overlapping roles of the inner ear and lateral line: the active space of dipole source detection. *Philosophical Transactions of the Royal Society of London*, 355:1115–1119, 2000.

[7] S. Coombs. Smart skins: Information processing by lateral line flow sensors. *Autonomous Robotics*, 11:255–261, 2001.

[8] S. Coombs and R. R. Fay. Dipole source localization by mottled sculpin, *Cottus bairdi*. *Journal of the Acoustical Society of America*, 93:2116–2123, 1993.

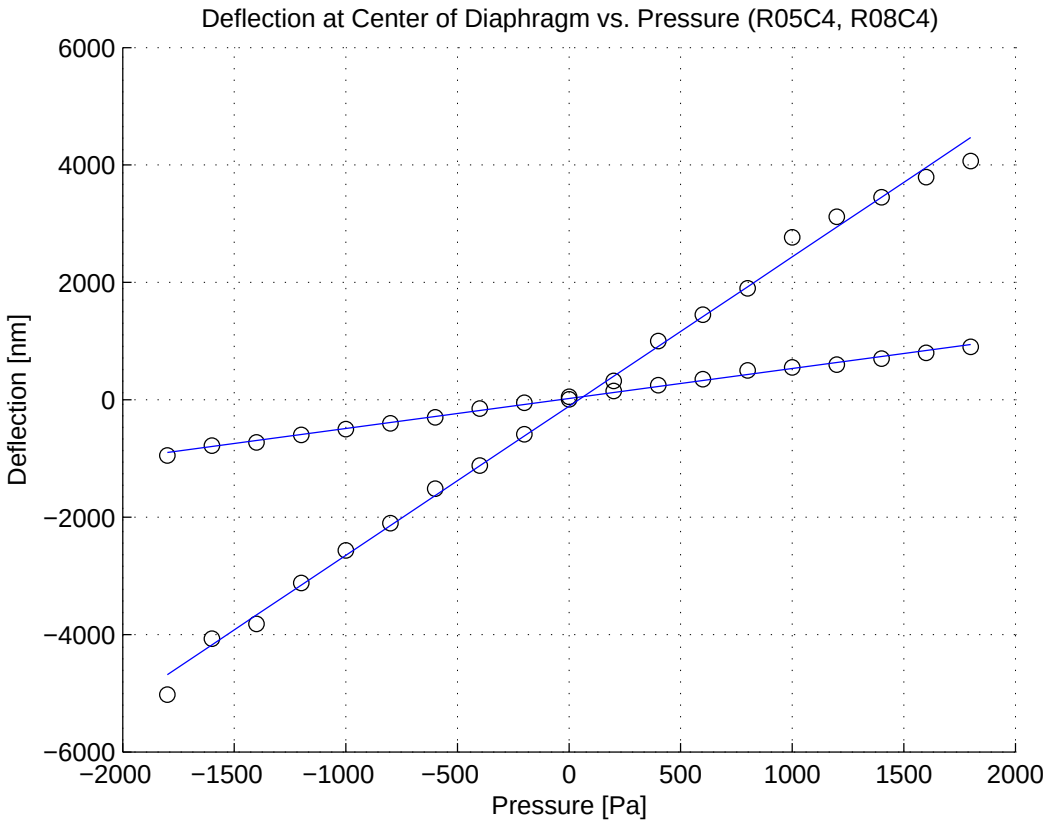

Figure 5: The deflection of the center of the membrane at various pressures for two different diaphragms. The steeper line results from a 2.828 mm diaphragm and the shallower line results from a 2 mm diaphragm. The circles represent data points and the solid lines represent the best-fit lines.

[9] H. Bleckmann, I. Waldner, and E. Schwartz. Frequency discrimination of the surface-feeding fish *Aplocheilus lineatus* - a prerequisite for prey localization? *Journal of Comparative Physiology A*, 143:485–490, 1981.

[10] M. A. Gibbs. Lateral line receptors: Where do they come from developmentally and where is our research going? *Brain, Behavior, and Evolution*, 64: 163–181, 2004.

[11] E. S. Hassan. Mathematical description of the stimuli to the lateral line system of fish derived from a 3-dimensional field analysis: I. the cases of moving in open water and of gliding towards a plane surface. *Biological Cybernetics*, 66:443–452, 1992.

[12] E. S. Hassan. Mathematical description of the stimuli to the lateral line system of fish derived from a 3-dimensional field analysis: II. the case of gliding alongside or above a plane surface. *Biological Cybernetics*, 66:453–461, 1992.

[13] E. S. Hassan. On the discrimination of spatial intervals by the blind cave fish (*Anoptichthys jordani*). *Journal of Comparative Physiology A*, 159:701–710, 1986.

[14] J. C. Montgomery, S. Coombs, and C. F. Baker. The mechanosensory lateral line system of the hypogean form of *Astyanax fasciatus*. *Evolutionary Biology of Fishes*, 62:87–96, 2001.

[15] J.C. Montgomery S.P. Windsor, D. Tan. Swimming kinematics and hydrodynamic imaging in the blind Mexican cave fish (Astayanax fasciatus). *Journal of Experimental Biology*, 211:2950–2959, 2008.

[16] J. N. Newman. *Marine Hydrodynamics*. MIT Press, Cambridge, Massachusetts, 1977.

[17] M. Ozgoren. Flow structure in the downstream of square and circular cylinders. *Flow Measurements and Instrumentation*, 17:225–235, 2005.

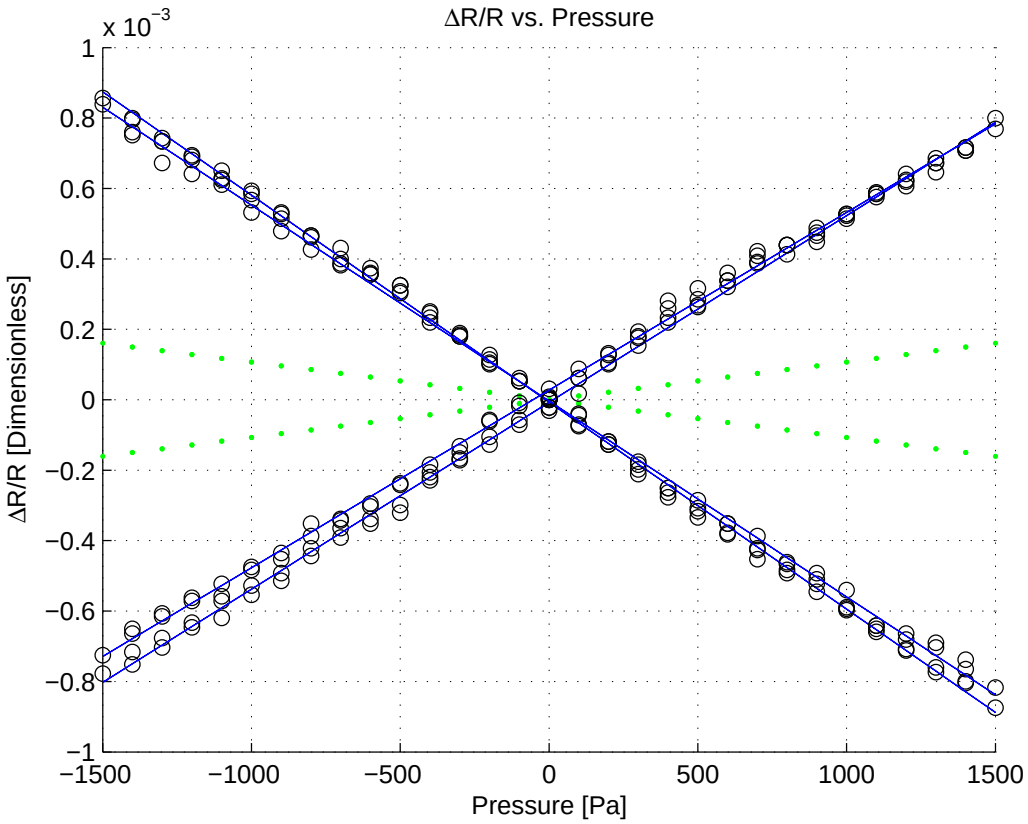

Figure 6: $\Delta R/R$ at various pressures for each of the four strain-gauge resistors on a particular diaphragm with width 2.82 mm. The circles represent data points, the solid lines represent the best-fit lines, and the dotted lines represents the theoretical data.

[18] K. Pohlmann, J. Atema, and T. Breithaupt. The importance of the lateral line in nocturnal predation of piscivorous catfish. *Journal of Experimental Biology*, 207:2971–2978, 2004.

[19] T. Suzuki and T. Colonius. Inverse-imaging method for detection of a vortex in a channel. *American Institute of Aeronautics and Astronautics Journal*, 41:1743–1751, 2003.

[20] C. von Campenhausen, I. Riess, and R. Weissert. Detection of stationary objects by the blind cave fish *Anoptichthys jordani* (Characidae). *Journal of Comparative Physiology*, 143:369–374, 1981.

[21] S. Theodoridis and K. Koutroumbas. *Pattern Recognition*. Academic Press, San Diego, California, third edition, 2006.

[22] I. T. Jolliffe. *Principal Component Analysis*. Springer, New York, New York, second edition, 2002.

[23] J. E. Jackson. *A User's Guide to Principal Components*. Wiley, Hoboken, New Jersey, 2003.

[24] J. Englemann, W. Hanke, J. Mogdans, and H. Bleckmann. Hydrodynamic stimuli and the fish lateral line. *Nature*, 408:51–52, November 2000.

[25] G. G. Harris and W. A. van Bergeijk. Evidence that the lateral line organ responds to near field displacements of sound sources in water. *Journal of Acoustical Society of America*, 34:1831–1841, 1962.

[26] S. Coombs, M. Hastings, and J. J. Finneran. Modeling and measuring lateral line excitation patterns to changing dipole source locations. *Journal of Comparative Physiology A*, 178:359–371, 1996.

[27] Y. Yang, J. Chen, J. Engel, S. Pandya, N. Chen, C. Tucker, S. Coombs, and C. Liu. Distant touch hydrodynamic imaging with an artificial lateral line. *Proceedings of the National Academy of Science*, 103(50):18891–18895, December 2006.

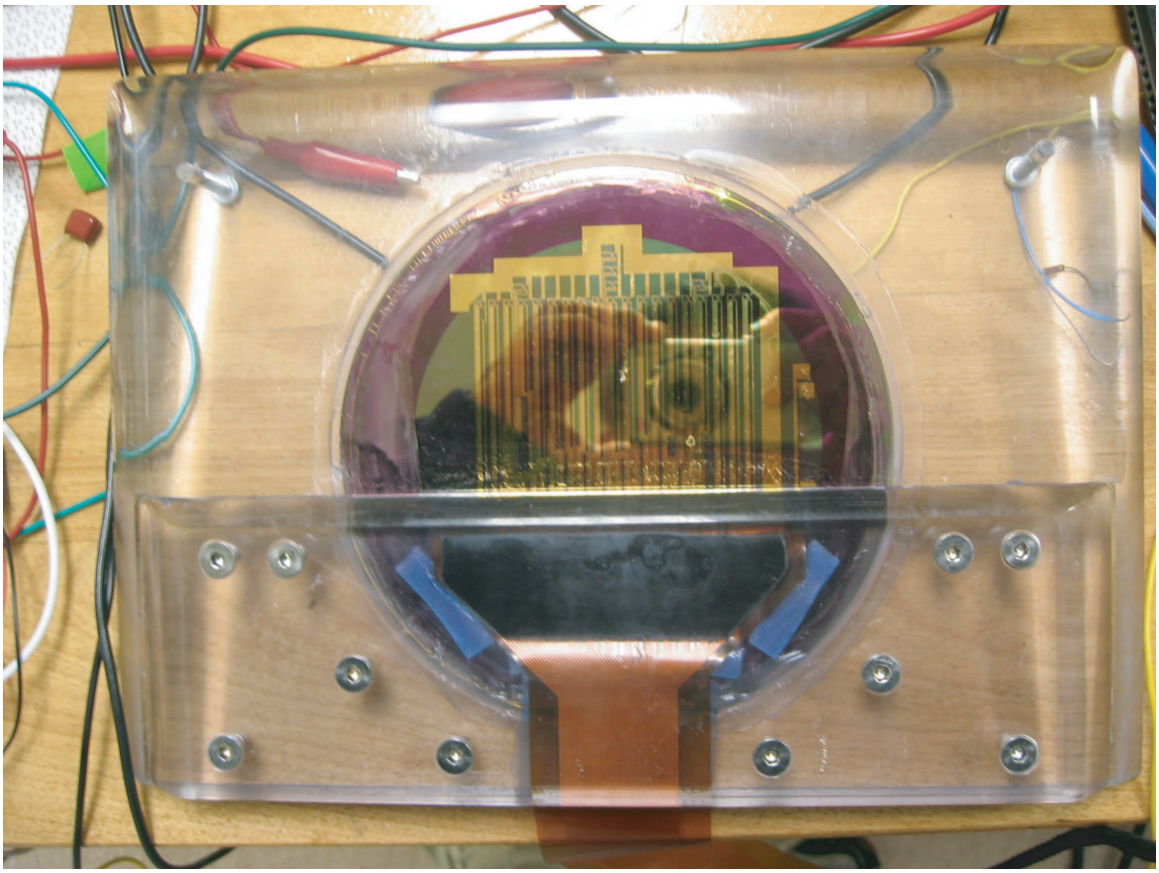

Figure 7: Photograph of a mounted wafer with pressure sensors that can used underwater. The wafer is 150 mm in diameter.

[28] Stephen M. Hou. A piezo-tunable gigahertz cavity microelectromechanical resonator. Master's thesis, Massachusetts Institute of Technology, Cambridge, Massachusetts, 2004.

[29] Lalitha Parameswaran. *Integrated Silicon Pressure Sensors Using Wafer Bonding Technology*. PhD thesis, Massachusetts Institute of Technology, Cambridge, Massachusetts, 1997.

[30] Lalitha Parameswaran. Silicon pressure sensors using wafer bonding technology. Master's thesis, Massachusetts Institute of Technology, Cambridge, Massachusetts, 1993.

[31] D. Vogel and H. Bleckmann. Behavioral discrimination of water motions caused by moving objects. *Journal of Comparative Physiology A*, 186:1107–1117, 2000.

[32] T. Teyke. Collision with and avoidance of obstacles by blind cave fish *Anoptichthys jordani* (characidae). *Journal of Comparative Physiology A*, 157: 837–843, 1985.

[33] R. Weissert and C. von Campenhausen. Discrimination between stationary objects by the blind cave fish *Anoptichthys jordani* (characidae). *Journal of Comparative Physiology A*, 143:375–381, 1981.